ENGINEERING

Graphene fatigue through van der Waals interactions

Teng Cui, Kevin Yip, Aly Hassan, Guorui Wang, Xingjian Liu, Yu Sun*, Tobin Filleter*

Graphene is often in contact with other materials through weak van der Waals (vdW) interactions. Of particular interest is the graphene-polymer interface, which is constantly subjected to dynamic loading in applications, including flexible electronics and multifunctional coatings. Through in situ cyclic loading, we directly observed interfacial fatigue propagation at the graphene-polymer interface, which was revealed to satisfy a modified Paris' law. Furthermore, cyclic loading through vdW contact was able to cause fatigue fracture of even pristine graphene through a combined in-plane shear and out-of-plane tear mechanism. Shear fracture was found to mainly initiate at the fold junctions induced by cyclic loading and propagate parallel to the loading direction. Fracture mechanics analysis was conducted to explain the kinetics of an exotic self-tearing behavior of graphene during cyclic loading. This work offers mechanistic insights into the dynamic reliability of graphene and graphene-polymer interface, which could facilitate the durable design of graphene-based structures.

INTRODUCTION

Graphene is the strongest material ever discovered both statically and dynamically, with an intrinsic strength of ~100 GPa (1) and a fatigue life of more than 10^9 cycles at ~5.6-GPa stress range and ~70-GPa mean stress levels (2). Van der Waals (vdW) interactions are among the weakest intermolecular forces, which are generally much weaker than intramolecular forces, such as covalent bonding (3). Scientifically, it is intriguing to investigate how the "strongest" material reacts in the presence of the "weakest" interaction. Furthermore, the wide applications of graphene involve contact with other materials through vdW interactions, among which the graphene-polymer interface is a primary example. A deep understanding of the vdW contact between polymer and graphene is important due to the wide existence of graphene-polymer interface in nanocomposites, sensors and detectors, multifunctional coatings, and flexible electronics (4–8), which are commonly subjected to complex mechanical loading. Previous studies have reported interfacial sliding of graphene on polymer substrates due to the low interfacial shear strength at the weak interface and wrinkling/buckling of graphene under compression of the substrate (9–11). These morphological patterns (e.g., wrinkles, buckles, and folds) of graphene formed on polymeric substrates have also been exploited for applications, such as nanofluidic channels and tuning surface wettability (12, 13). However, previous work has focused on the quasi-static loading or unloading effect on the graphene morphology. There is a lack of detailed dynamic investigation, such as fatigue, on the interfacial and structural evolution of graphene and graphene-polymer interface under cyclic loading.

To achieve high reliability and robustness of graphene and graphene-polymer interface, several fundamental questions must be addressed. Is a graphene-polymer interface susceptible to progressive fatigue damage? Can pristine graphene exhibit fatigue fracture rather than mere morphological instability (e.g., wrinkles and buckle delamination) by pure vdW interactions? If so, then what are the fracture modes and contributing failure mechanisms? Here, via in situ cyclic loading, we show that pure vdW interactions at the graphene-polymer interface can induce substantial fatigue

fracture of graphene through a combination of in-plane shear and out-of-plane tear mechanisms. In addition, direct evidence of interfacial fatigue damage propagation before the main fracture event was also observed. The cyclic damage evolution kinetics was analyzed. These results deepened the understanding on the dynamic stability of graphene, which could potentially facilitate the design of durable graphene-based flexible electronics, multifunctional coatings, and nanocomposites.

RESULTS

Interfacial fatigue damage propagation

Fatigue damage of various materials and structures under different stress states has long been a concern. Typical fatigue experiments include cyclic tension, shear, and bending of both homogeneous materials and composites to investigate both the intrinsic and interfacial fatigue behavior. Conventionally, the fatigue resistance of materials is characterized by the crack growth rate (i.e., crack elongation per cycle, da/dN) under a fixed stress range ($\Delta\sigma$) during cyclic loading. For ductile solids, there are three typical regimes of crack propagation, i.e., Regime A, the near-threshold slow-growth rate; Regime B, mid-growth rate, also known as the Paris regime; and Regime C, near-failure high-growth rate, among which Regime B has been investigated most intensively (14). The fatigue crack growth behavior in Regime B has commonly been described by the Paris' law, which states that da/dN scales with the stress intensity factor range (ΔK) by the power law relationship $\frac{da}{dN} = c(\Delta K)^m$, where c and m are fitting parameters, and $\Delta K = \Delta\sigma\sqrt{\pi a}$ with $\Delta\sigma$ representing the applied stress range, and a is the half crack length. Interfacial fatigue of various contacts has also been investigated through multiple approaches, including, but not limited to, cyclic pullout tests, lap-shear tests, and peeling tests, with the main damage behavior identified as sliding and delamination at the interfaces (15–17). However, interfacial fatigue behavior of the vdW contacts between graphene and its substrates remains largely unexplored. Because of the two-dimensional (2D) nature, and thus ultralow bending stiffness (18, 19), graphene is susceptible to out-of-plane buckling, especially at the contact of a stretchable substrate with elastic mismatch. These uniqueness implies different forms of fatigue damage and damage dynamics as compared to the fatigue fracture propagation in macroscale, and the macroscopic methods and analyses are also not readily applicable.

Department of Mechanical and Industrial Engineering, University of Toronto, Toronto, ON M5S3G8, Canada.
*Corresponding author. Email: sun@mie.utoronto.ca (Y.S.); filleter@mie.utoronto.ca (T.F.)

To probe the interfacial fatigue behavior of the graphene-polymer contact, we mechanically exfoliated graphene films onto a stretchable polydimethylsiloxane (PDMS) substrate, which was subjected to uniaxial cyclic loading; meanwhile, the dynamic evolution of the graphene was recorded in situ under an optical microscope, as illustrated in Fig. 1A. Figure 1B shows the morphological changes of graphene after various cycles (labeled as C#) under a cyclic strain range $\Delta\varepsilon = 5\%$ and strain ratio $R = \frac{\varepsilon_{min}}{\varepsilon_{max}} = 0$. Periodic wrinkles and local buckle delamination, identified as black lines, formed and propagated inward during cyclic loading/unloading (see also movie S1). We confirmed that the optically identified black lines are buckles using atomic force microscopy (AFM) in Fig. 1C and high-magnification optical imaging in fig. S1. The wider white belts are collapsed folds, which are more clearly revealed later in Fig. 2 and fig. S2. The

buckle formation near the graphene edges was caused by interfacial sliding during the loading stage and consequent compression during unloading (9, 20). Thin-film buckling theories (21) predicted that the periodic wrinkles (conformal deformation of the film and substrate) are energetically more favorable than buckle delamination (separation between the film and the substrate) due to the substantial elastic modulus mismatch between graphene and PDMS (~5 × 10^5 : 1). With further increases in the compressive stress on the graphene during the unloading stage, buckle delamination was observed to be locally activated alongside the existing wrinkles and grew into a collapsed fold. This wrinkle-to-fold transition in 2D materials has also been reported during the release of a prestretched substrate in the literature (22). In the current study, more local delamination and folds were activated with increasing cycles due to
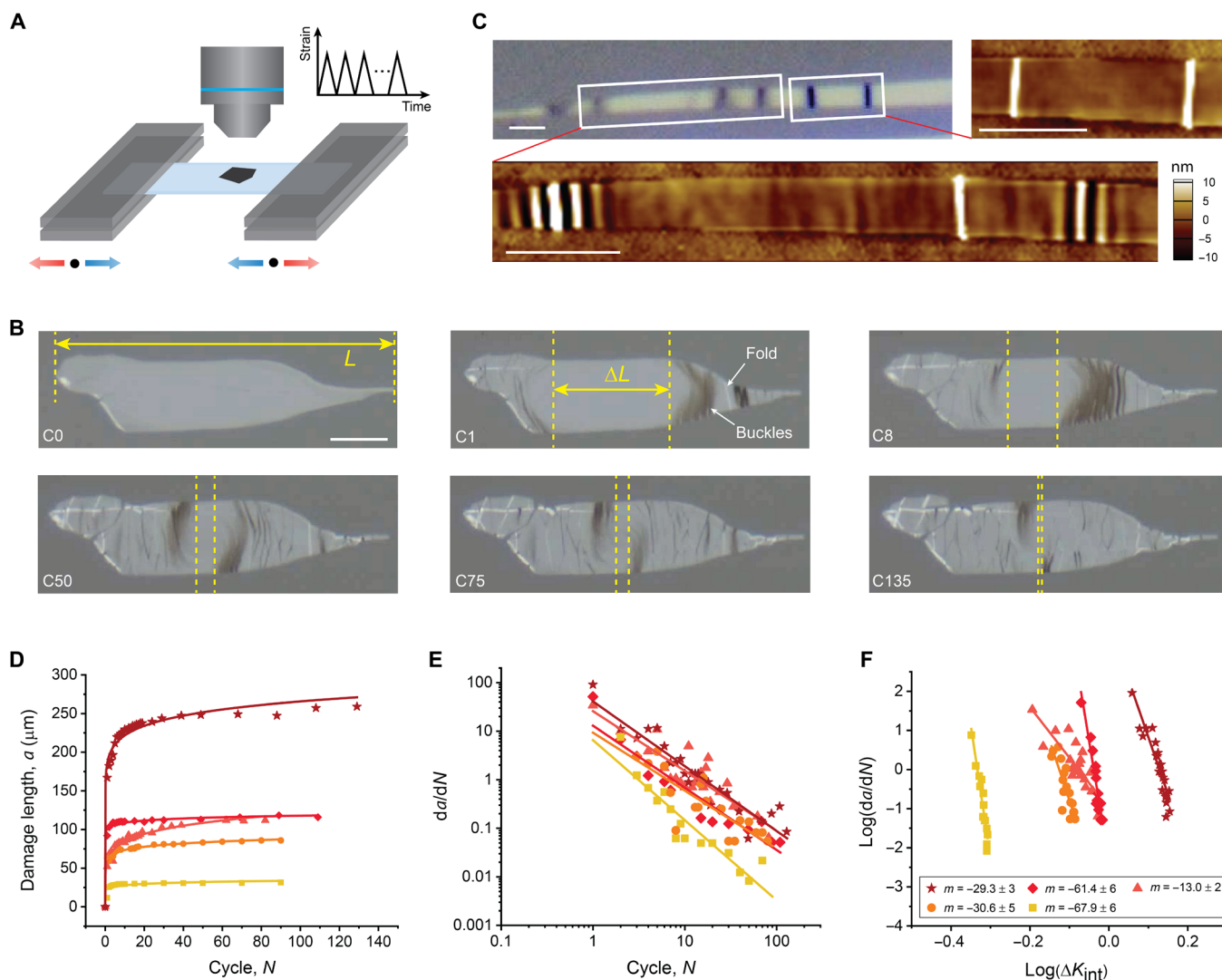

Fig. 1. Propagation of interfacial damage zone under cyclic loading. (**A**) Schematic of cyclic loading setup. The polymer substrate is loaded cyclically where the two jaws move simultaneously outward and inward to maintain the graphene in the center for in situ observation. Inset shows a schematic of the triangular cyclic strain profile. (**B**) Real-time optical images showing the propagation of buckling zone after different fatigue cycles under strain range $\Delta\varepsilon = 5\%$ and strain ratio $R = 0$. (**C**) AFM images of buckles that appear as black lines optically. (**D** and **E**) Damage length, a, and its propagation rate, $\frac{da}{dN}$, as a function of fatigue cycle, both exhibiting a power law relation. The damage length eventually approaches the total length of the sample. (**F**) The damage propagation rate as a function of interfacial strain intensity factor range, ΔK_{int}, showing that the propagation of graphene-polymer interfacial fatigue damage can be described by a modified Paris' law as in Eq. 3. Values of m were extracted by curve fitting with SEs. Scale bars, 50 (B) and 5 μm (C).
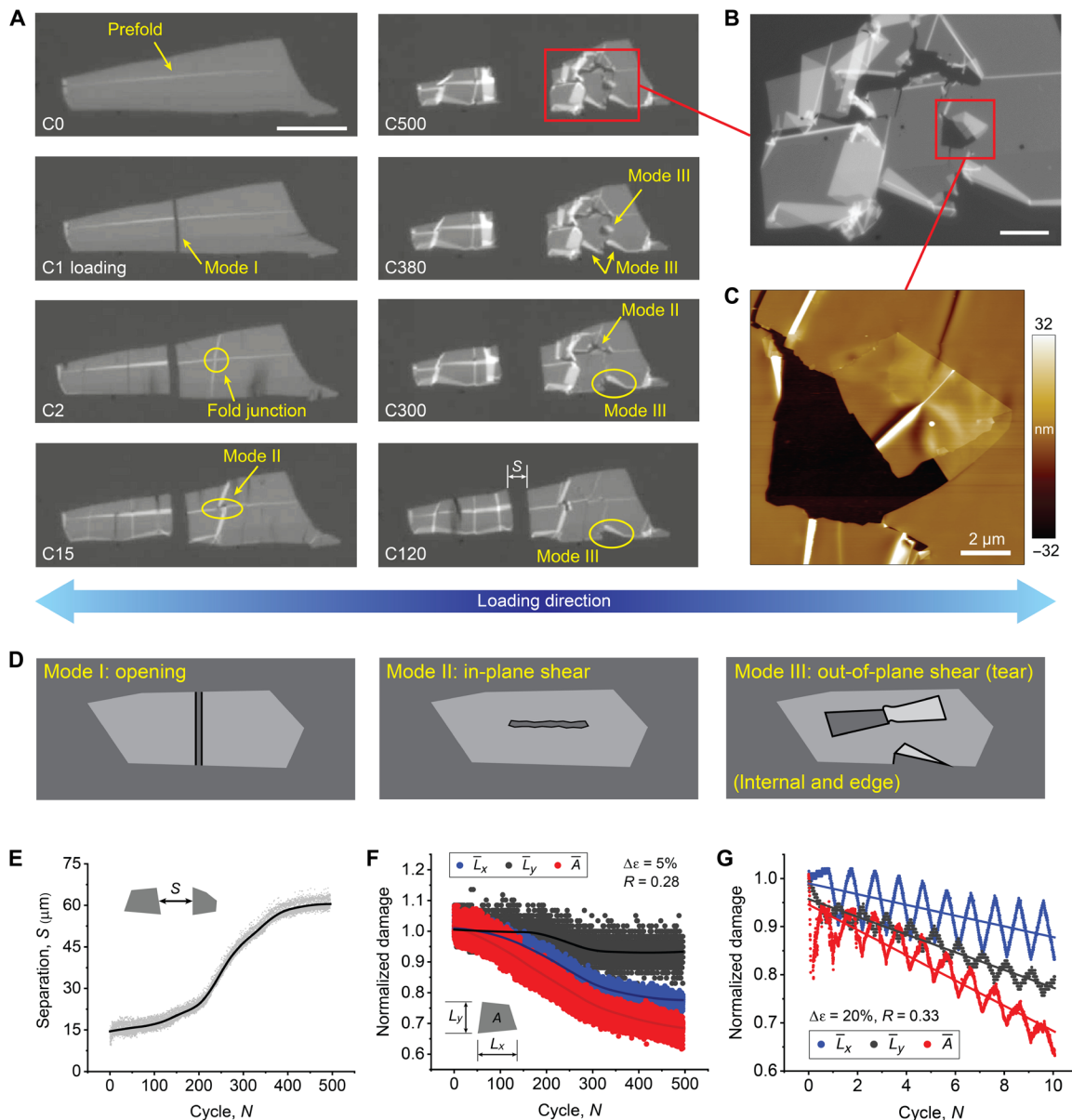
Fig. 2. Mixed-mode fatigue fracture and damage of graphene. (**A**) Time-lapsed images showing the multiple fracture modes of graphene. Mode I fracture (opening cleavage) was perpendicular to the loading direction and was not caused by fatigue. Mode II fracture (in-plane shear) initiated at a fold junction and propagated along the loading direction (C15 to C500). Mode III fracture (tear) occurred at both edge and internal defective sites. (**B**) High-magnification image of the damaged graphene after 500 fatigue cycles, showing details of folds, tears, and cracks. (**C**) AFM topographic image of an internal tear in (B). (**D**) Schematics of the three different fracture modes observed in the experiments. (**E**) Separation distance between the two graphene films, showing sigmoidal behavior with cycle number. (**F**) Evolution of normalized area and lengths in both directions with cycle number, showing similar sigmoidal behavior. (**G**) Normalized damage of graphene under large strain range $\Delta\varepsilon = 20\%$ and $R = 0.33$, highlighting local oscillation of area and lengths during cyclic loading. Scale bars, 50 (A), 10 (B), and 2 μm (C).

the repeated sliding at the interface, which degraded the contact quality and lowered the critical buckling strain. It is also noted that because of the edge effect, the wrinkles appeared curved along the width direction. On the basis of quasi-static analysis, if the system is stretched to a fixed loading strain, then the unloading-induced buckling zone is also fixed and determined by whether the local strain in the graphene reaches the critical value (*23*). However, in the current study under cyclic loading, even with a fixed strain range, we observed that the buckle wave fronts dynamically propagated

toward the internal region, and there was a wrinkle-to-fold transition thereafter in the buckling zone. These phenomena provide direct evidences and visualization of the interfacial damage propagation at the graphene-polymer interface under cyclic loading.

To analyze the damage propagation kinetics, we assign 1D undamaged zone ΔL and total length L (Fig. 1C) and then define the total damage length $a = L - \Delta L$. The buckle wave front was optically identified by setting a consistent contrast threshold in an imaging processing tool. Because of the optical diffraction limit and image

processing parameters, there exists a systematic error of ~1 µm in the detection of the buckle wave front as compared to the AFM measured position. However, the absolute position does not affect the buckle propagation rate substantially. Figure 1D shows that the damage length a propagates in a power law relation with cycle number N and eventually approaches the total length of the sample

$$a = c_1 N^{m_1} \tag{1}$$

where c_1 and m_1 are scaling parameters. Thus, the damage propagation rate, $\frac{da}{dN}$, also follows the power law relation with N

$$\frac{da}{dN} = c_1 m_1 N^{m_1-1} \tag{2}$$

as also validated by the linear relation between $\frac{da}{dN}$ and N in a double logarithmic plot shown in Fig. 1E. Combining Eqs. 1 and 2 and rearranging the constants leads to

$$\frac{da}{dN} = c\left(\Delta\varepsilon \sqrt{\pi a}\right)^m \tag{3}$$

In Eq. 3, c and m are a new set of fitting parameters related to c_1 and m_1, and a newly introduced parameter $\Delta\varepsilon$ is the applied substrate strain range, which is a constant during each test (see details in the Supplementary Materials). Here, we define an interfacial strain intensity factor $K_{int} = \varepsilon \sqrt{\pi a}$, which is an analog to the stress intensity factor $K = \sigma \sqrt{\pi a}$, but with a representing the interfacial damage length in the K_{int} and half crack length in K. ε here is the applied substrate strain. On the basis of this definition, the interfacial fatigue propagation rate $\frac{da}{dN}$ can be expressed in terms of the range of interfacial strain intensity factor ΔK_{int} as in Eq. 3, which is analogous to the Paris' law. Similar to conventional fatigue studies, the applied $\Delta\varepsilon$ should be large enough to initiate and propagate buckling damage; however, if $\Delta\varepsilon$ is too large, then the entire graphene piece would be damaged within one cycle.

Figure 1F reveals that the graphene-polymer interfacial fatigue damage can be well described by the modified Paris' law (Eq. 3). Fitting the data in Fig. 1F by Eq. 3 yields values of m ranging from −13.0 to −67.9. The wide range of m is likely due to the variation of contact quality, which is critical for the buckling behavior but is hard to control during sample preparation due to its stochastic nature and atomic-scale thickness. A previous study has also reported a nonhomogeneous contact between exfoliated graphite and PDMS substrate using atomic force acoustic microscopy (24). Therefore, it could be difficult to achieve high-level consistency quantitatively across samples. However, despite the across-sample variations, all the samples followed the same damage propagation kinetics. We also note that this model is applicable for 1D fatigue damage propagation, and the damage caused along the (in-plane) perpendicular direction should be limited to avoid notable interference.

It is interesting to reveal that classical fatigue cracks propagate at an increasing rate with cycles ($m > 0$), eventually leading to fast unstable fracture. However, here, the interfacial fatigue damage propagation rate decreases with cycles ($m < 0$), with the fastest damage occurring in the first cycle, which exhibits reverse damage kinetics as compared to the classical fatigue crack growth. Such a reverse trend is attributed to the drastically different fatigue damage mechanisms. In the current study, the buckle delamination generated in the first cycle resulted in a smaller middle contact region of graphene with

the substrate. The damage propagation was maintained by the following loading/unloading cycles, which continued to induce sliding/buckling at the edges of the smaller intact region. Energetically, once a buckling zone is formed, the energy input from later cycles is largely dissipated at the existing buckling zone by forming larger buckles and folds, thus leading to a decrease in the rate of creating new damage zones. In contrast, for classical uniaxial tensile loading of cracked solids, the energy release rate G increases with the crack length, which drives faster crack propagation.

Mixed-mode fatigue fracture of graphene

In addition to the interfacial fatigue damage propagation, we show that pristine graphene can also suffer fracture by cyclic loading through weak vdW interactions. Previous studies (13, 25–27) have demonstrated that chemical vapor–deposited graphene can easily fracture by loading or unloading the polymeric substrates due to its high defect density. The presence of preexisting defects could substantially decrease the strength and fracture strain of graphene (28, 29). Figure 2 presents a mixed-mode fatigue fracture of mechanically exfoliated graphene through interfacial loading at the graphene-polymer contact ($\Delta\varepsilon = 5\%$, $R = 0.28$). In few cases, we noticed that even in the loading stage of the first cycle (C1 loading), the graphene film cleaved into two clean pieces, which is a typical signature of Mode I fracture. In fracture mechanics, as illustrated in Fig. 2D, Mode I fracture refers to the opening mode where the applied stress is normal to the crack surface. Mode II fracture is designated as the fracture caused by in-plane shear where the shear stress is parallel with the crack line. Mode III fracture is caused by out-of-plane shear or tear where the shear stress at the crack front is normal to the 2D material's surface. Here, the Mode I fracture was simply caused by monotonic loading to failure at low tensile strain (2.7%). Here, we focused on the fatigue fracture of graphene caused by cyclic loading. Ten samples have been tested and analyzed. This representative sample (Fig. 2A) has a prefold caused by pretensioning of the PDMS substrate. The subsequent cycles generated more folds both vertically and horizontally, forming multiple junctions. It was consistently observed that fracture occurred and preferred to initiate at the fold junctions but unexpectedly propagated along the loading direction. As imaged after 15 cycles (C15 in Fig. 2A), the vertical fold split in two at the junction and further separated horizontally, which is a typical Mode II fracture of the graphene. Previous work on Mode II damage in graphene focused on the interfacial debonding between graphene and various substrates under quasi-static loading (30, 31). There is still a lack of experimental report on the shear-induced fracture of graphene itself, both statically and dynamically. The Mode II fatigue fracture at the junction can be of particular concern, especially for applications that make use of buckle networks for trapping or administering fluids (12) and creating superhydrophobic surfaces (13). Further fatigue loading resulted in Mode III fracture, including both edge tear (C120) and internal tear (C380). Figure 2B shows a higher magnification image of the graphene film after 500 cycles, and an AFM topography image of the internal tear is shown in Fig. 2C. Schematics of the three fracture modes are illustrated in Fig. 2D.

To quantify the cyclic loading effect, the configurational changes of graphene were tracked dynamically frame by frame, including the separation between two graphene films S and changes in area A and lengths L_x and L_y. As summarized in Fig. 2E, the separation distance S increases with cycles, showing a sigmoidal behavior. The

separation was enlarged at an increasing rate up to ~250 cycles and then followed by a gradual decreasing rate to approximately zero. The widening of the two films is a manifest of graphene-polymer interfacial sliding. The area and lengths evolution in Fig. 2F were normalized by dividing the initial values before loading, and they revealed a similar sigmoidal behavior but in a decreasing trend. These results showed that the fatigue degradation of graphene was not at a constant rate. At the initial stage, the graphene films had fewer fractured regions and buckle delamination. The generation of any new cracks and buckles serves as initiation sites for more folds and cracks, which, in turn, accelerates the fatigue damage. However, once the graphene shrank to a certain extent, further folding of the (thicker) shrunken structure became more difficult and required more energy. The decreasing contact size between graphene and substrate also reduced the strain transferred to the graphene film. Therefore, the damage process was decelerated at later stages, since the cyclic loading was conducted at a fixed strain amplitude (i.e., fixed energy input). Moreover, fatigue testing at larger mean strains and strain amplitudes was also conducted. Figure 2G is an example of fatigue loading at $\Delta\varepsilon = 20\%$, showing 30% of area reduction in just 10 cycles, which took 500 cycles for loading at $\Delta\varepsilon = 5\%$ (Fig. 2E). Although both area and lengths were decreasing globally during cyclic loading, there were still oscillations in these two quantities within each cycle, and the oscillations followed the cyclic loading frequency. As shown in Fig. 2G, loading of the substrate horizontally led to a local increase in L_x and a local decrease in L_y due to Poisson's effect; the reverse is true for unloading. Calculating the effective Poisson's ratio ($\nu_{eff} = -\frac{\Delta\varepsilon_y}{\Delta\varepsilon_x}$) for both loading and unloading stages yields 0.46 and 0.25, respectively. Because of the fact that there was out-of-plane deformation involved, the Poisson's ratios calculated here are not intrinsic properties of the graphene and that also explains why both values are higher than the intrinsic graphite's Poisson's ratio of 0.165 in the basal plane (32). The higher effective ν_{eff} during the loading stage as compared to the unloading stage is a result of permanent buckling (delamination or folds) and energy dissipation during the fatigue cycles. An additional example of fatigue fracture at an even larger strain range ($\Delta\varepsilon = 50\%$) is provided in the Supplementary Materials (figs. S4 and S5). In that case, it is interesting to observe the PDMS substrate fractured during the cyclic process, and the fast retraction of the substrate resulted in substantially more and denser buckles on graphene than previous cycles, indicating that the interfacial delamination process could be strain rate sensitive. However, a detailed understanding of the strain rate sensitivity still requires further investigation.

Fatigue fracture mechanisms

To understand the mechanisms of the two main fatigue fracture modes, in-plane shear and tear, we conducted AFM characterization on the junctions of folds and performed an energy-based fracture mechanics analysis on the tears. Figure 3A shows three AFM topography images on the folds and junctions of a graphene film that has undergone 10 cycles of loading ($\Delta\varepsilon = 20\%$, $R = 0.33$). These AFM images revealed the complexity of the deformation, featuring knotted junctions formed by multiple folds, cross junctions formed by two perpendicular folds, and hierarchical buckles (wrinkles on folds). These complex fold junctions induced severe stress concentration, as revealed by previous atomistic simulations (13, 33). Furthermore, the coexistence of vertical and horizontal folds dissected the graphene film into multiple small islands bordered by the folds (Fig. 3B). At the folds, the strain in graphene was mostly relaxed by the out-of-plane deformation (34). Since the out-of-plane folds effectively resulted in lower global in-plane stiffness and the stress transfer efficiency is also lower at the buckles (35), the motion/deformation of each small region was more independent and noncoherent due to geometrical asymmetry and edge effect. Previous study on Raman mapping of graphene revealed highly nonuniform strain distributions when applying substrate strain of higher than even 0.6% (36). The noncoherent deformation at the adjacent edge of the fold boundary resulted in shear along the fold, which is consistent with previous molecular dynamics simulations (37, 38). Therefore, the cracks initiated at the junctions where the stress is highly concentrated and propagated along the loading axis under cyclic loading, as illustrated in Fig. 3B. We also observed that the shear cracks could propagate along one or both directions of the fold, as shown in Fig. 3 (C and D).

Another prominent fatigue fracture mode observed was tearing, as previously shown in Fig. 2 (A to C). Figure 4A is another example showing the snapshots of an internal tear propagation. The tearing process propagated in a fast, nonstable manner (see movies S2 and S3), and the torn graphene ribbon later stopped at a topographic barrier (e.g., another fold). The tear length c and area were measured during the tearing process and plotted in Fig. 4B. Here, the tear length refers to the longer side of the tear, as indicated in Fig. 4A. Figure 4C shows an outline of the final tear with the central red line indicating the tear propagation direction. Both the tearing direction and width were dynamically changing, which is distinct from the previously observed self-tearing behavior of graphene on SiO₂ substrates by Annett and Cross (39). In their work, small prefolds in graphene were artificially created by a nanoindenter, and then the self-tearing at the folds spontaneously occurred along a fixed propagation direction and stopped at a fixed tear width due to thermal activation. Here, small tears in the form of prefold tabs were commonly formed at both the edges and internal defects or cracks (Figs. 2A and 3C) due to cyclic loading–induced out-of-plane deformation. Another fundamental difference from the self-tearing of graphene on SiO₂ substrate is the additional applied force on graphene through the interface in this study. To understand the tear propagation mechanism with the application of external loading, such as why the tear propagation direction and tear width change, we performed an energy-based fracture mechanics analysis. Considering a tear situation as shown in the schematic of Fig. 4D, without external loading, Annett and Cross (39) showed that the total energy change of the system can be expressed as

$$U = U_e + 2\lambda c + (\gamma_1 - \gamma_2) A_{tear} \tag{4}$$

where U_e is the elastic energy of the fold due to bending at the tear front; λ is the fracture energy of graphene per unit crack length; c is the tear crack length; γ_1 and γ_2 are the graphene/PDMS and graphene/graphene adhesion energy, respectively; and A_{tear} represents the area of the tear. The forces along the tear edges can be expressed as the energy release rate along the tear crack direction

$$F_c = -\frac{\partial U}{\partial c} = 2DS\sin\theta - 2\lambda + (\gamma_2 - \gamma_1)w\cos\theta \tag{5}$$

where D is the bending stiffness, S is a constant relating to the bending configuration of the fold, θ is the half taper angle of the tear, and w is the crack width at the tear front. The force F_c contains both
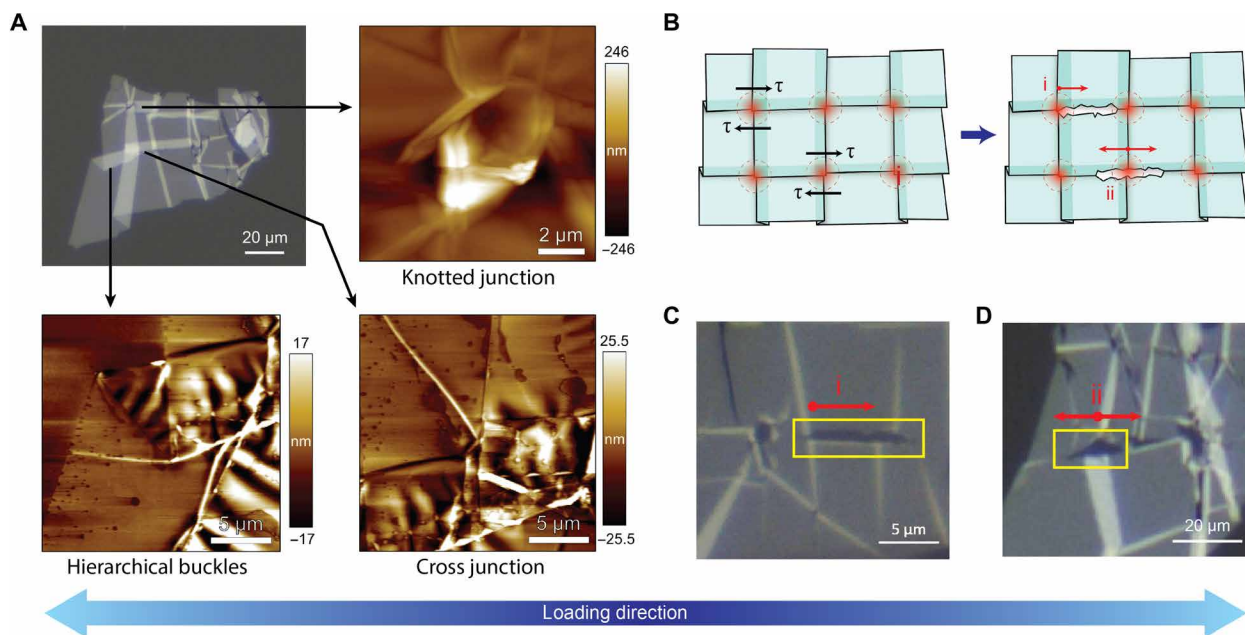
Fig. 3. Fatigue fracture by in-plane shear at fold junctions. (**A**) AFM topography images of cyclically loaded graphene showing the geometrical complexity of folds and junctions. (**B**) Schematics showing the mechanism of junction shear. Shear fracture initiated at the cyclic loading–induced fold junctions due to severe stress concentration. The shear crack could propagate along (i) one or (ii) both sides of the fold, as shown in examples (**C**) and (**D**), respectively.
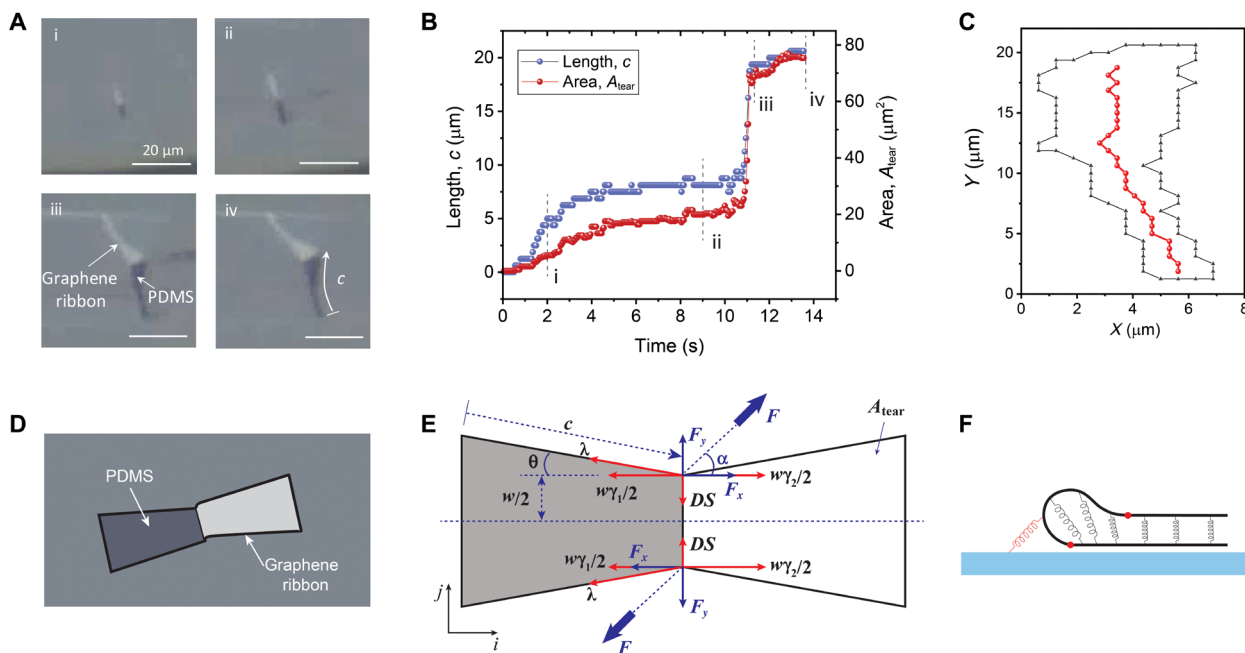

Fig. 4. Fatigue fracture by tearing. (**A**) Snapshots of an internal tear propagation at different stages. (**B**) Tear length and area as a function of time showing unstable propagation, with the four stages in (A) indicated in the timeline. (**C**) Outline of the final tear with midline showing the change of tear width and propagation direction. (**D**) Schematic of a tear with external loading. (**E**) Top view of the tear schematic with acting forces on the tear front. (**F**) Cross-sectional view of the tear schematic highlighting graphene/graphene adhesion as an advancing force and graphene/PDMS adhesion as a resistance force.

advancing force and resistance force at the two edges of the tear ($F_c = 2F_{advancing} - 2F_{resistance}$). At each edge of the tear front (Fig. 4E), $F_{advancing} = \frac{\gamma_2 w\cos\theta}{2} + DS \sin\theta$, and $F_{resistance} = \frac{\gamma_1 w\cos\theta}{2} + \lambda$. According to the literature, γ_2 is ~300 mJ/m^2 (40) and γ_1 is ~7 mJ/m^2 (41). Without external loading, the driving force originates from the

adhesion energy difference between the graphene/graphene interaction and graphene/PDMS interaction (Fig. 4F); and the resistance force stems from the fracture energy (λ) required to tear the graphene. It is also noted that the sliding friction at the graphene-graphene interface must also be very low for the self-tearing mechanism to

occur, likely in a state of superlubricity due to incommensurate stacking, as suggested by a previous scanning Raman spectroscopy study (*39*).

In the case of our experiments, the graphene sample was constantly subjected to external loading F (F_x, F_y: horizontal, vertical component) from the substrate, and the external force could be of any angle α to the current tear propagation direction, as illustrated in Fig. 4E. If $\alpha = 90°$, the external force is perpendicular to tearing propagation direction, i.e., $F_x = 0$, then at the equilibrium state

$$\frac{(\gamma_2 - \gamma_1)\,w}{2} = \lambda\cos\theta \qquad (6)$$

$$DS = \lambda\sin\theta + F_y \qquad (7)$$

From Eq. 7, it can be deduced that the taper angle θ could be tuned by varying F_y. Moreover, θ could also be negative when $F_y > DS$, and the tear width w at equilibrium could also be altered accordingly based on Eq. 6. Under the current angle convention, θ is positive when tapering inward. Figure 4A is an example of an outward taper at a large loading force. Since F was constantly changing during the experiment, the taper angle was also changing dynamically, as revealed in Fig. 4C. From an energy standpoint, because of the additional strain energy input to the host graphene from the PDMS substrate, the torn ribbon needs to further enlarge its contact area with the host graphene, i.e., by increasing the tear width. By doing so, there would be larger region transformed from highly strained host graphene to lightly strained torn ribbon, which allows more energy to be released. This is also in line with the tendency of minimizing its internal energy by having a larger overlapping region. If $\alpha \neq 90°$, which is the most common situation, then the pair of F_x component at the tear front would act as a force couple with a moment of magnitude $F_x w$. The system does not reach equilibrium until the force couple drives the tear propagating toward the direction where F is perpendicular to the tear propagation ($F_x = 0$). This also explains why the tear in Fig. 4A (tear outline in Fig. 4C) followed a curving path and eventually ended normal to the loading direction. Our results demonstrated that mechanical oscillation of an elastic substrate provides another route to trigger self-tearing of the adhered graphene. The detailed tear propagation behavior could also be tuned by the external force through a mechano-thermally driven mechanism. Edge tearing is similar in mechanism with only one fracture path. However, it is noted that the real situation is more complicated, and the wrinkles and buckle delamination may interfere and affect the tearing propagation. The model assumes a uniform contact quality between graphene and PDMS substrate for simplicity.

DISCUSSION
Here, we have conducted in situ cyclic loading of graphene-loaded polymer and directly observed interfacial fatigue damage propagation at the graphene-polymer interface and vdW-induced fatigue fracture of graphene. In addition to the well-known graphene buckling phenomenon due to elastic strain mismatch, we found that cyclic loading not only induces but also dynamically propagates the affected buckling zone from near the edges to the internal region and that the propagation is well described by a modified Paris' law. Configurational analysis revealed that the damage evolution of graphene

follows a sigmoidal behavior, featuring a nonconstant damage rate. Furthermore, this work highlights the striking effect of interface on the mechanical behavior of graphene under cyclic loading. Although graphene has the highest intrinsic strength and fatigue life, the dynamic involvement of vdW interactions at the interface fractures the graphene through in-plane shear and out-of-plane tear fracture mechanisms. These results offer mechanistic insights into the dynamical mechanical behavior of graphene in nanocomposites and multifunctional coatings. Proper fatigue behavior needs to be evaluated and controlled in those applications for extended lifetime. Moreover, our theoretical analysis suggests that external loading of the substrate offers a possible route for more tunable self-assembly and mass transport of graphene by controlling the tearing propagation characteristics, such as taper angle and propagation direction. The developed theoretical framework and fracture behavior could also be extended to other 2D materials on various stretchable substrates.

MATERIALS AND METHODS
Samples and characterization
PDMS (Dow SYLGARD 184) with a substrate of thickness ~0.8 mm was prepared by mixing the prepolymer base with curing agent at a ratio of 10:1, followed by 1 hour curing at 110°C. Then, graphene with a ranging thickness from 1.70 to 3.24 nm was mechanically exfoliated from bulk graphite (NGS Naturgraphit) directly onto the PDMS substrate. The thickness was measured by tapping mode AFM across a fold of the graphene itself. Direct imaging across the PDMS-graphene step would result in notable error due to the drastically different tip interactions between PDMS and graphene. Cyclic loading of the substrate was conducted using a microtensile tester (Deben), and the fatigue cycles were implemented in displacement control at a constant strain rate of 2.5×10^{-3}/s, during which the dynamic process was observed in situ in an optical microscope (Zeiss Scope A1). All the AFM (Asylum Research) topography images were obtained in tapping mode using a sharp silicon tip ($k = 42$ N/m, $f = 330$ kHz).

Optical image processing
The videos of the graphene-polymer system undergoing fatigue testing were analyzed with the Image Processing Toolbox in MATLAB. Within the region of interest, each frame was converted into a grayscale image, and a threshold in pixel intensity was used to differentiate the graphene from the background polymer. With the graphene region identified, the length in x and y was measured by using a bounding box around the graphene. The area was calculated by counting the number of pixels in the graphene region. The gap separation between two graphene pieces was calculated by taking an average of all the distances between the pieces along the horizontal x direction. All measurements were then converted into microns by using the scale bar in the video as a pixel-to-micron ratio.

SUPPLEMENTARY MATERIALS
Supplementary material for this article is available at http://advances.sciencemag.org/cgi/content/full/6/42/eabb1335/DC1

REFERENCES AND NOTES
1. C. Lee, X. Wei, J. W. Kysar, J. Hone, Measurement of the elastic properties and intrinsic strength of monolayer graphene. *Science* **321**, 385–388 (2008).
2. T. Cui, S. Mukherjee, P. M. Sudeep, G. Colas, F. Najafi, J. Tam, P. M. Ajayan, C. V. Singh, Y. Sun, T. Filleter, Fatigue of graphene. *Nat. Mater.* **19**, 405–411 (2020).

3. J. N. Israelachvili, in *Intermolecular and Surface Forces*, J. N. Israelachvili, Ed. (Academic Press, San Diego, ed. 3, 2011), pp. 253–289.

4. M. A. Rafiee, J. Rafiee, Z. Wang, H. Song, Z. Yu, N. Koratkar, Enhanced mechanical properties of nanocomposites at low graphene content. *ACS Nano* **3**, 3884–3890 (2009).

5. M. A. Rafiee, A. V. Thomas, A. Zandiatashbar, J. Rafiee, N. A. Koratkar, W. Lu, J. M. Tour, N. A. Koratkar, Graphene nanoribbon composites. *ACS Nano* **4**, 7415–7420 (2010).

6. N. Liu, A. Chortos, T. Lei, L. Jin, T. R. Kim, W.-G. Bae, C. Zhu, S. Wang, R. Pfattner, X. Chen, R. Sinclair, Z. Bao, Ultratransparent and stretchable graphene electrodes. *Sci. Adv.* **3**, e1700159 (2017).

7. W. Zhu, D. B. Farmer, K. A. Jenkins, B. Ek, S. Oida, X. Li, J. Bucchignano, S. Dawes, E. A. Duch, P. Avouris, Graphene radio frequency devices on flexible substrate. *Appl. Phys. Lett.* **102**, 233102 (2013).

8. P. Kang, M. C. Wang, P. M. Knapp, S. W. Nam, Crumpled graphene photodetector with enhanced, strain-tunable, and wavelength-selective photoresponsivity. *Adv. Mater.* **28**, 4639–4645 (2016).

9. T. Jiang, R. Huang, Y. Zhu, Interfacial sliding and buckling of monolayer graphene on a stretchable substrate. *Adv. Funct. Mater.* **24**, 396–402 (2014).

10. L. Gong, I. A. Kinloch, R. J. Young, I. Riaz, R. Jalil, K. S. Novoselov, Interfacial stress transfer in a graphene monolayer nanocomposite. *Adv. Mater.* **22**, 2694–2697 (2010).

11. G. Wang, E. Gao, Z. Dai, L. Liu, Z. Xu, Z. Zhang, Degradation and recovery of graphene/polymer interfaces under cyclic mechanical loading. *Compos. Sci. Technol.* **149**, 220–227 (2017).

12. M. G. Pastore Carbone, A. C. Manikas, I. Souli, C. Pavlou, C. Galiotis, Mosaic pattern formation in exfoliated graphene by mechanical deformation. *Nat. Commun.* **10**, 1572 (2019).

13. J. Zang, S. Ryu, N. Pugno, Q. Wang, Q. Tu, M. J. Buehler, X. Zhao, Multifunctionality and control of the crumpling and unfolding of large-area graphene. *Nat. Mater.* **12**, 321–325 (2013).

14. S. Suresh, *Fatigue of Materials* (Cambridge Univ. Press, ed. 2, 1998).

15. D. P. Walls, F. W. Zok, Interfacial fatigue in a fiber reinforced metal matrix composite. *Acta Metall. Mater.* **42**, 2675–2681 (1994).

16. M. Hojo, Y. Matsushita, M. Tanaka, T. Adachi, Interfacial fatigue crack propagation in microscopic model composite using bifiber shear specimens. *Compos. Part A Appl. Sci. Manuf.* **43**, 239–246 (2012).

17. J. Liu, S. Lin, X. Liu, Z. Qin, Y. Yang, J. Zang, X. Zhao, Fatigue-resistant adhesion of hydrogels. *Nat. Commun.* **11**, 1071 (2020).

18. E. Han, J. Yu, E. Annevelink, J. Son, D. A. Kang, K. Watanabe, T. Taniguchi, E. Ertekin, P. Y. Huang, A. M. Van Der Zande, Ultrasoft slip-mediated bending in few-layer graphene. *Nat. Mater.* **19**, 305–309 (2020).

19. G. Wang, Z. Dai, J. Xiao, S. Feng, C. Weng, L. Liu, Z. Xu, R. Huang, Z. Zhang, Bending of multilayer van der Waals materials. *Phys. Rev. Lett.* **123**, 116101 (2019).

20. G. Wang, Z. Dai, L. Liu, H. Hu, Q. Dai, Z. Zhang, Tuning the interfacial mechanical behaviors of monolayer graphene/PMMA nanocomposites. *ACS Appl. Mater. Interfaces* **8**, 22554–22562 (2016).

21. H. Mei, R. Huang, J. Y. Chung, C. M. Stafford, H. H. Yu, Buckling modes of elastic thin films on elastic substrates. *Appl. Phys. Lett.* **90**, 151902 (2007).

22. J. Yu, S. Kim, E. Ertekin, A. M. Van Der Zande, Material-dependent evolution of mechanical folding instabilities in two-dimensional atomic membranes. *ACS Appl. Mater. Interfaces* **12**, 10801–10808 (2020).

23. C. J. Brennan, J. Nguyen, E. T. Yu, N. Lu, Interface adhesion between 2D materials and elastomers measured by buckle delaminations. *Adv. Mater. Interfaces* **2**, 1500176 (2015).

24. K. Yip, T. Cui, T. Filleter, Enhanced sensitivity of nanoscale subsurface imaging by photothermal excitation in atomic force microscopy. *Rev. Sci. Instrum.* **91**, 063703 (2020).

25. D. Rhee, J. T. Paci, S. Deng, W. K. Lee, G. C. Schatz, T. W. Odom, Soft skin layers enable area-specific, multiscale graphene wrinkles with switchable orientations. *ACS Nano* **14**, 166–174 (2020).

26. H. Jang, Z. Dai, K.-H. Ha, S. K. Ameri, N. Lu, Stretchability of PMMA-supported CVD graphene and of its electrical contacts. *2D Mater.* **7**, 014003 (2020).

27. J. H. Lee, D. W. Jang, S. G. Hong, B. C. Park, J. H. Kim, H. J. Jung, S. B. Lee, Fracture mechanism and electromechanical behavior of chemical vapor deposited graphene on flexible substrate under tension. *Carbon* **118**, 475–484 (2017).

28. P. Zhang, L. Ma, F. Fan, Z. Zeng, C. Peng, P. E. Loya, Z. Liu, Y. Gong, J. Zhang, X. Zhang, P. M. Ajayan, T. Zhu, J. Lou, Fracture toughness of graphene. *Nat. Commun.* **5**, 3782 (2014).

29. X. Zhao, D. G. Papageorgiou, L. Zhu, F. Ding, R. J. Young, The strength of mechanically-exfoliated monolayer graphene deformed on a rigid polymer substrate. *Nanoscale* **11**, 14339–14353 (2019).

30. G. Guo, Y. Zhu, Cohesive-shear-lag modeling of interfacial stress transfer between a monolayer graphene and a polymer substrate. *J. Appl. Mech.* **82**, 031005 (2015).

31. Z. Cao, L. Tao, D. Akinwande, R. Huang, K. M. Liechti, Mixed-mode traction-separation relations between graphene and copper by blister tests. *Int. J. Solids Struct.* **84**, 147–159 (2016).

32. O. L. Blakslee, D. G. Proctor, E. J. Seldin, G. B. Spence, T. Weng, Elastic constants of compression-annealed pyrolytic graphite. *J. Appl. Phys.* **41**, 3373–3382 (1970).

33. K. Zhang, M. Arroyo, Understanding and strain-engineering wrinkle networks in supported graphene through simulations. *J. Mech. Phys. Solids* **72**, 61–74 (2014).

34. Z. Li, I. A. Kinloch, R. J. Young, K. S. Novoselov, G. Anagnostopoulos, J. Parthenios, C. Galiotis, K. Papagelis, C. Y. Lu, L. Britnell, Deformation of wrinkled graphene. *ACS Nano.* **9**, 3917–3925 (2015).

35. Z. Li, R. J. Young, D. G. Papageorgiou, I. A. Kinloch, X. Zhao, C. Yang, S. Hao, Interfacial stress transfer in strain engineered wrinkled and folded graphene. *2D Mater.* **6**, 045026 (2019).

36. R. J. Young, L. Gong, I. A. Kinloch, I. Riaz, R. Jalil, K. S. Novoselov, Strain mapping in a graphene monolayer nanocomposite. *ACS Nano* **5**, 3079–3084 (2011).

37. Y. Tian, Z. Li, W. Gao, K. Cai, F. Wang, D. Zhang, B. Shirinzadeh, S. Fatikow, Mechanical properties investigation of monolayer h-BN sheet under in-plane shear displacement using molecular dynamics simulations. *J. Appl. Phys.* **115**, 014308 (2014).

38. T. Ragab, J. McDonald, C. Basaran, Aspect ratio effect on shear modulus and ultimate shear strength of graphene nanoribbons. *Diamond Relat. Mater.* **74**, 9–15 (2017).

39. J. Annett, G. L. W. Cross, Self-assembly of graphene ribbons by spontaneous self-tearing and peeling from a substrate. *Nature* **535**, 271–275 (2016).

40. P. Li, Z. You, T. Cui, Adhesion energy of few layer graphene characterized by atomic force microscope. *Sens. Actuators A Phys.* **217**, 56–61 (2014).

41. S. Scharfenberg, D. Z. Rocklin, C. Chialvo, R. L. Weaver, P. M. Goldbart, N. Mason, Probing the mechanical properties of graphene using a corrugated elastic substrate. *Appl. Phys. Lett.* **98**, 091908 (2011).

Citation: T. Cui, K. Yip, A. Hassan, G. Wang, X. Liu, Y. Sun, T. Filleter, Graphene fatigue through van der Waals interactions. *Sci. Adv.* **6**, eabb1335 (2020).